CORE
Metadata, citation and similar papers at core.ac.uk
Provided by IntechOpen

We are IntechOpen, the world's leading publisher of Open Access books Built by scientists, for scientists

4,800
Open access books available

122,000
International authors and editors

135M
Downloads

Our authors are among the

154
Countries delivered to

TOP 1%
most cited scientists

12.2%
Contributors from top 500 universities

WEB OF SCIENCE™

Selection of our books indexed in the Book Citation Index in Web of Science™ Core Collection (BKCI)

Interested in publishing with us?
Contact book.department@intechopen.com

Numbers displayed above are based on latest data collected.
For more information visit www.intechopen.com

1

BST and Other Ferroelectric Thin Films by CCVD and Their Properties and Applications

Yongdong Jiang, Yongqiang Wang, Kwang Choi
Deepika Rajamani and Andrew Hunt
nGimat Co.
U.S.A

1. Introduction

Ferroelectric materials, such as $BaTiO_3$ (BTO), $Pb(Zr,Ti)O_3$ (PZT), $SrBi_2Ta_2O_9$ (SBT), and $LiNbO_3$ (LNO), are a category of materials with reorientable spontaneous polarization, a sub-category of pyroelectric materials. Because of their high dielectric constant, large polarization, and high breakdown voltage, ferroelectric materials have a wide range of applications, including infrared (IR) detectors for security systems and navigation, high density capacitors, high-density dynamic random access memory (DRAM), non-volatile ferroelectric random access memory (FRAM), and high frequency devices such as varactors, frequency multipliers, delay lines, filters, oscillators, resonators and tunable microwave devices (Tagantsev, et al., 2003; Cole, et al., 2000; Bao, et al., 2008; Gevorgian, et al., 2001; Dawber, et al., 2005).

Among these ferroelectric materials, BTO based films with Sr dopant, namely $Ba_{1-x}Sr_xTiO_3$ (BST) are the most investigated one for various applications, especially for electric field response (or tunable) components and devices because of its high dielectric constant, reasonable dielectric loss, high tunability, and large breakdown strength. The Curie temperature T_c can be easily adjusted by controlling the Ba to Sr ratio. Studies have revealed that the electrical properties of BST films are influenced by the deposition and post-deposition process, stoichiometry, electrodes, microstructure, thickness, surface roughness, oxygen vacancies in films, and film homogeneity. The composition of the BST film such as the (Ba+Sr)/Ti ratio plays a critical role in determining its electrical properties (Y. H. Xu, 1991; Takeuchi, et al., 1998; Im, et al., 2000). Both the dielectric constant and loss increased with increasing (Ba+Sr)/Ti ratio. The lowest loss tangent (0.0047) and the best figure of merit were achieved with a (Ba+Sr)/Ti ratio of 0.73, but tunability was diminished (Im, et al., 2000). *n*Gimat has also optimized the elemental ratios to achieve some of the highest figures of merit in tunable devices using the enhancements thus optimized.

It has also been reported that dopants influence the electrical properties of BST thin films, but all dopants negatively affect at least one of the desired properties of the solicitation (Copel, et al., 1998 and Chung, et al., 2008). Copel and coworkers (Copel, et al., 1998) investigated the effect of Mn on electrical properties of BST thin films and found that leakage current was improved by introducing Mn. This was attributed to the acceptor Mn

doping increasing the depletion width in BST films and the barrier for thermionic emission from a Pt contact into the BST film. Takeuchi and coworkers (Takeuchi, et al., 1998) studied several BST dopants using their combinatorial synthesis technique. The experimental results showed that both W and Mn in small amounts reduced the leakage current dramatically while only slightly decreasing dielectric constant. It was theorized that the W substituted for Ti as a donor and suppressed the formation of oxygen vacancies. *n*Gimat has studied numerous dopants and uses dopants in almost all applications.

Although much success has been made in optimizing physical properties of uniform composition FE materials, especially BST, for various applications, these materials still suffer from decreased performance such as low tunability and high loss in high frequency range. Therefore, compositionally graded and multilayered FE thin films have been attracting much attention in past few years (Zhong, et al., 2007; Misirlioglu, et al., 2007; Katiyar, et al., 2005; Kang, et al., 2006; Pintilie, et al., 2006; Lu, et al., 2008; Liu, et al., 2007; Heindl, et al., 2007). As an example, Zhong (Zhong, et al., 2008) deposited multilayered BST films on Pt/Si substrates. The multiplayer heterostructures consisted of three distinct layers with Ba/Sr ratios of 63/37, 78/22, and 88/12. The first composition is paraelectric while the last two are ferroelectric at room temperature. The film structure has a dielectric constant of 360 with a dielectric loss of 0.012 and a tunability of 65% at 444 kV/cm. These properties exhibited minimal dispersion between –10 and 90°C. As known, while the dielectric loss in BST films can be greatly reduced by various dopants, tunability of monolithic BST is strongly dependent on the temperature. Multilayer and graded FEs display little temperature dependence due to the variations in T_C that results in a diffuse phase transformation. The tunability can be maximized by optimizing the internal electric fields that arise between layers due to the polarization mismatch. *n*Gimat's tunable materials normally consists of at least two compositional layers, with one being <10nm thick.

This chapter covers the following areas: introduction to the CCVD process, depositions and properties of BST, PZT, and $CaCu_3Ti_4O_{12}$ thin films, and fabrication and performance of tunable microwave devices based on BST thin films.

2. Introduction to CCVD

Combustion Chemical Vapor Deposition (CCVD) (Andrew, et al., 1993, 1997, 1999) is an open atmosphere deposition process in which the precursors are dissolved in a solvent, which typically also acts as the combustible fuel. This solution is then atomized to form submicron droplets, which are then conveyed by an oxygen-containing stream to the flame using the Nanomiser® device. In CCVD of thin films, the substrate is coated by simply drawing it over the flame plasma, as shown Figure 1. The flame provides energy required for the precursors to react and to vapor deposit on the substrate. Substrate temperature is an independent process parameter that can be varied to actively control the deposited film's microstructure. Although flame temperatures are usually in excess of 800 °C, the substrate may dwell in the flame zone only briefly, thus remaining cool (<100°C). Alternatively, the substrate can be either allowed to rise in temperature or easily cooled in the open atmosphere. *n*Gimat has utilized its patented CCVD process in depositing over 100 distinct materials compositions for a variety of applications. Due to the inherent compositional flexibility of the NanoSpray Combustion Process, we can fabricate thin films, nanopowders, and composites from a wide range of metals, ceramics, and polymers, as illustrated by the examples in Table 1.

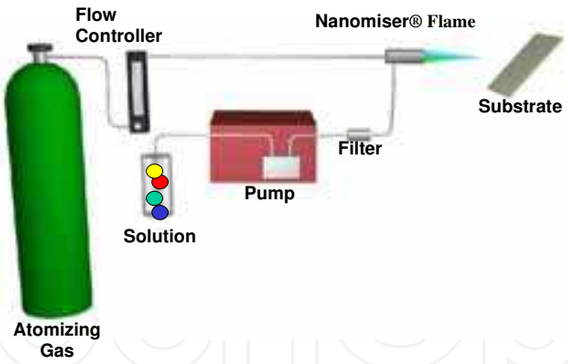

Fig. 1. Schematic of the CCVD system, the thin film NanoSpray combustion process

Metal	Ceramics	Composites
Ag, Au, Cu, Ir, Ni, Rh, Pt, Zn.	Complex oxides: $(Ba,Sr)TiO_3$, $(Pb,La)(Zr,Ti)O_3$, $(La,Sr)CoO_3$, $Pb(Mg,Nb)O_3$, Spinels, $YBa_2Cu_3O_x$, $YbBa_2Cu_3O_x$, $LaAlO_3$, ITO, $Y_3Fe_5O_{12}$, $SrRuO_3$, ZrO_2, Simple oxides: Al_2O_3, SiO_2, Ta_2O_5, In_2O_3, ZnO, ZrO_2, V_2O_5, WO_3, CeO_2, Cr_2O_3, Cu_xO, Fe_2O_3, MgO, Mn_2O_3, MoO_3, Nb_2O_5, NiO, RbO_x, RhO_x, RuO_2, TiO_2	Polymer/metal Polymer/ceramic Ceramic/metal
Substrates Used		
Single crystal ceramics: Si, sapphire, $LaAlO_3$, MgO, $SrTiO_3$, yttrium stabilized ZrO_2, quartz Polycrystalline ceramics: SiC, Si_3N_4, Al_2O_3, silica Metals: platinized Si wafers, Cu, Al, Ag, Pt, Ni, steel, NiCr, superalloys, Ti, TiAl alloy Polymers: Nafion™, Teflon™, polycarbonate		
Applications		
Capacitors, resistors, catalytic applications, corrosion resistance, electronics, engines, ferroelectrics, solar cells, fuel cells, optics, piezoelectrics, buffer layers, superconductors, thermal barrier, thermal control, and wear resistance		

Table 1. Partial list of materials deposited by CCVD

3. Depositions of ferroelectric thin films by CCVD

Many ferroelectric materials, such as BST and PZT, have been deposited successfully by the CCVD technique. These ferroelectric thin films are grown epitaxially on sapphire, single crystal MgO, and single crystal $SrTiO_3$ (STO) substrates.

3.1 Depositions of BST thin films by CCVD and their properties

Compared to polycrystalline or textured thin films, epitaxial dielectric thin films show higher dielectric breakdown and lower dielectric loss. Therefore, epitaxial thin films are preferred for many applications, especially for high frequency microwave applications. Single layer BST and multilayer dielectric thin films have been successfully deposited on sapphire (both *c*- and *r*-orientations). Figure 2 shows typical plan view and cross sectional images on a single layer BST thin film of *c*-sapphire substrate by CCVD. The film is dense and smooth with uniform grains and thickness. Figure 3 shows an area detector XRD pattern and a (110) pole figure of a typical BST thin film on *c*-sapphire. Epitaxy can be determined in about 15 min by area

detector XRD. The sample is rotated continuously in ϕ and scanned in ω during signal collection so that all peaks are excited. The (006) plane of sapphire is parallel to the substrate surface and perpendicular to the θ/2θ direction. 2θ increases from the right side to the left side. The area detector XRD pattern shows that there are only (111) peak of the BST film and (006) peak of sapphire along the θ/2θ direction. The (110) and (111) peaks of the BST film appear as dots and align with (104) and (006) peaks of sapphire, showing the BST film was grown epitaxially on *c*-sapphire substrate. The epitaxiy of the BST film is further confirmed by the (110) pole figure as shown in Figure 3 (b). Pole figure measurement is a powerful method to determine the in-plane alignment between the epitaxial film and its substrate in a relatively large area. BST (110) reflections were selected to perform the pole figure collection and to detect the presence of the in-plane alignment because of its large 2θ separation from the sapphire (104) plane. As shown in Figure 3 (b), six sharp spots of the BST (110) reflections with narrow intensity distribution were observed every 60^{o} along the ϕ direction. These results indicate clearly that the BST thin film was epitaxially grown on *c*-sapphire substrate and has (111) plane parallel to the substrate surface. The orientation relationship between the BST film and *c*-sapphire substrate is BST (111)//sapphire (0001) and BST [110]//sapphire [104]. The pole figure measurements suggest a type (2) or type (3) epitaxial growth of BST film on *c*-sapphire substrate (Baringay & Dey, 1992).

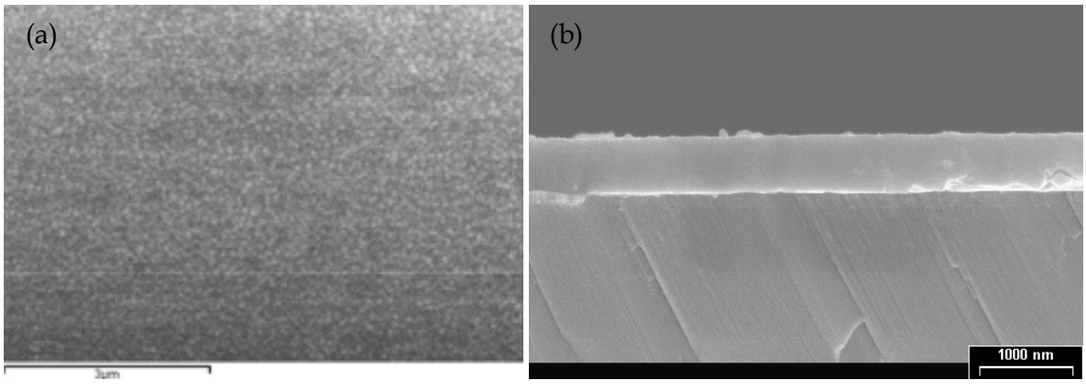

Fig. 2. SEM (a) plan view and (b) cross section images of typical BST thin films by CCVD

Inter-digital capacitors (IDC) with an 8 μm gap between electrodes and co-planar waveguide (CPW) structures were fabricated on the epitaxial BST dielectric thin films by the lift-off process. Dielectric properties were measured on the IDC structures at 1 MHz by a HP 4285A LCR meter. Its tuning and dielectric loss as a function of applied voltage are present in Figure 4. The tuning increases while the dielectric loss decreases with the increase of applied voltage. At an applied voltage of 40 V (which is the limit of the instrument), a tuning of 51% and a dielectric loss of 0.0046 were achieved. The dielectric constant of the film is about 1150.

In addition to single layer BST dielectric thin films, nanostructured multilayer dielectric thin films with alternative ferroelectric and paraelectric phases with a thickness in nanometer range have also been successfully deposited onto various single crystal substrates including *c*-sapphire, single crystal MgO, and single crystal STO, et al. Figure 5 shows the SEM image and area detector XRD pattern of a multilayer dielectric thin film with 36 alternative ferroelectric and paraelectric nano-layers and a total thickness of 500 nm. The film is dense and smooth with uniform fine grains. The XRD pattern shows that the (110) and (111) peaks

of the multilayer dielectric film appear as dots, aligning with (104) and (006) peaks of sapphire (the (006) plane is parallel to the substrate surface), showing the multilayer dielectric film was grown epitaxially on the *c*-sapphire substrate as single layer thin films.

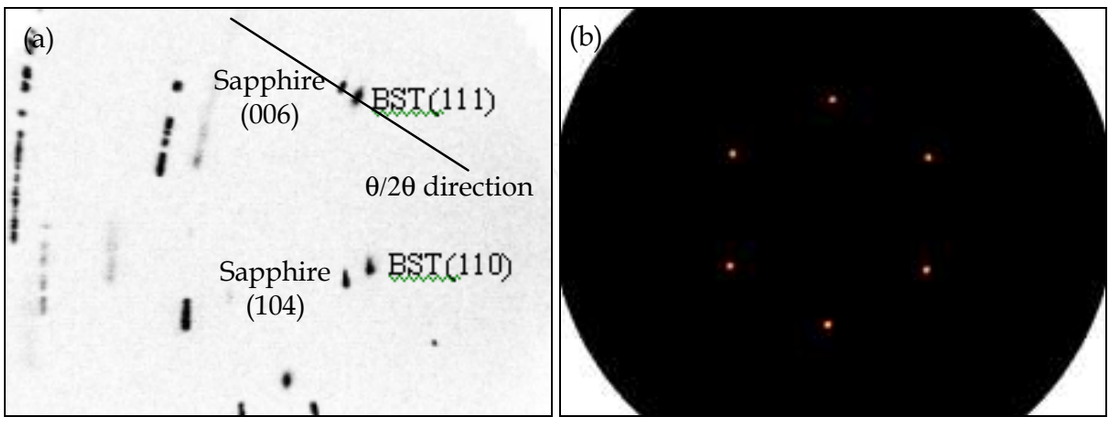

Fig. 3. (a) Area detector XRD pattern and (b) (110) pole figure of a typical single layer BST film on *c*-sapphire substrate

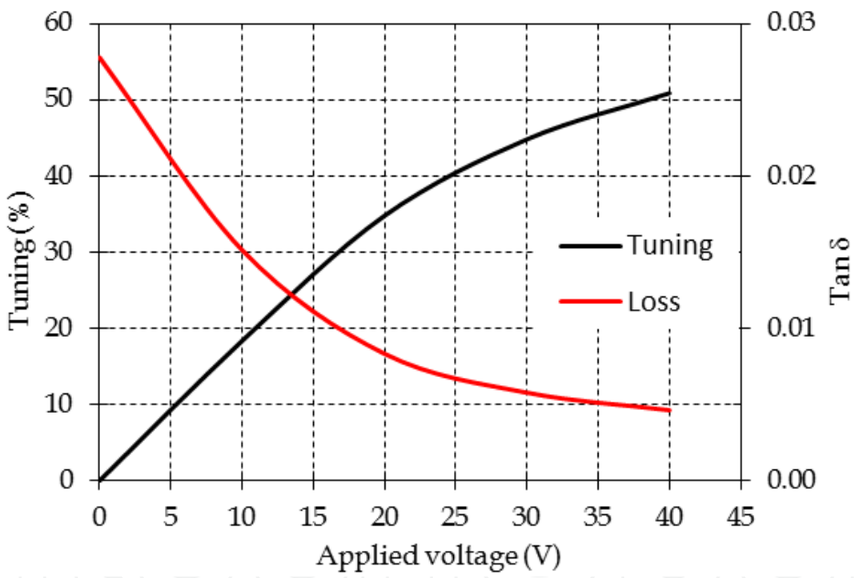

Fig. 4. Tuning and dielectric loss of a single layer BST film on *c*-sapphire substrate as a function of applied voltage

The same IDC and CPW structures were fabricated on the multilayer thin films. The dielectric and microwave properties of a selected multilayer thin film and a standard single layer film are summarized in Table 2. The multilayer thin film has a slightly lower capacitance at 1 MHz compared to the standard single layer film. However, its dielectric loss at 1 MHz and 0 V is about 0.005, which is much lower than that of the single layer thin film (0.028). The figure of merit (FOM), which is defined as (tuning × capacitance)/loss tangent, of the multilayer film is about 3 times as high as that of the standard single layer film. The high FOM and low dielectric loss benefit the applications for high frequency and high power microwave devices.

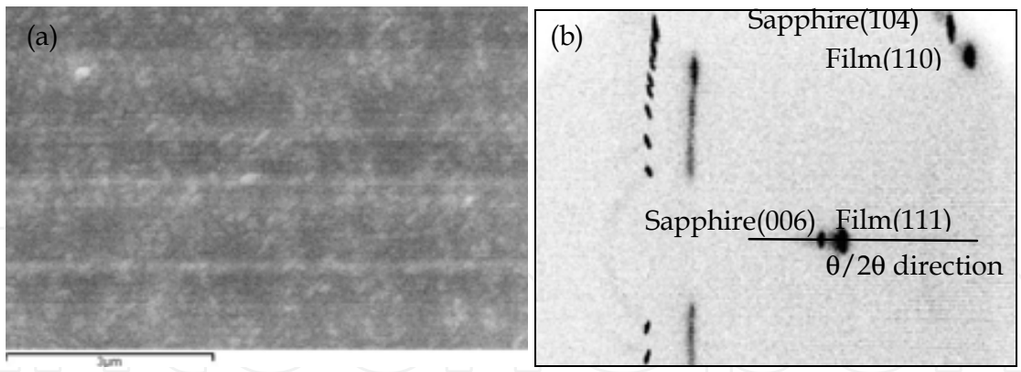

Fig. 5. (a) SEM image and (b) XRD pattern of a multilayer dielectric thin film

Sample ID	Capacitance and loss at 1 MHz				S_{21} at 50 GHz (dB)	Tuning (%)	FOM
	0 V		40 V				
	Cp (pF)	Tanδ	Cp (pF)	Tanδ			
Multilayer	1.14	0.005	0.90	0.003	1.46	21.1	4820
Single layer	1.28	0.028	0.85	0.019	-	33.3	1537

Table 2. Comparison of electrical properties between a multilayer and a single layer film

The tunable BST dielectric thin films, both single layer and multilayer, have been scaled up to 2″ round sapphire wafers. For depositing BST thin films on 2″ wafers, the substrate is maintained at a uniform temperature in a furnace. The substrate rotates on a vacuum chuck and the flame impacts the wafer at a 45° angle through a cutout on the side of the furnace, in which smooth and dense epitaxial thin films are deposited, as shown in Figure 6.

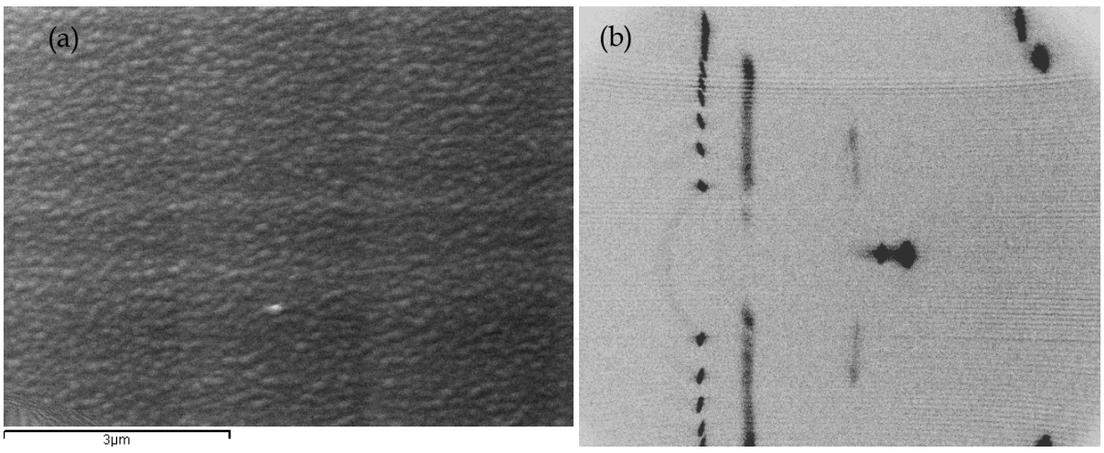

Fig. 6. (a) SEM image and (b) area detector XRD pattern of a BST thin film on 2" *c*-sapphire wafer

3.2 Depositions of PZT thin films by CCVD and their properties

Lead-based ferroelectric materials such as lead zirconate titanate ($Pb(Zr,Ti)O_3$, PZT), a member of the perovskite structure family, is a solid solution of lead titanate ($PbTiO_3$, PTO) and lead zirconate ($PbZrO_3$, PZO) with different Zr/Ti ratios. It is well known that their

physical properties can be modified by changing the Zr/Ti ratio and substituting a part of Pb ion by tri-valent ions. Among the tri-valent dopants, lanthanum (La) has been found the most suitable element for increasing the density and other physical properties of the materials (Rukmini et al., 1999; Dimos et al., 1994). PZT and La doped PZT ($Pb_{1-x/100}La_{x/100}(Zr_{y/100}Ti_{z/100})O_3$, PLZT x/y/z) have been extensively investigated for applications, such as DRAM (Hwang et al., 1999; H. H. Kim et al., 1998), FRAM (Ramash et al., 2001; W. S. Kim et al., 1999), sensors and actuators for microelectromechanical systems (MEMS)(B. M. Xu, 1999; Polla and Francis, 1998), infrared detectors (Song et al., 2001; Kobune et al., 2001), due to their excellent dielectric, ferroelectric, piezoelectric, and pyroelectric properties. PLZT is transparent in the visible and near infrared region of the electromagnetic waves and has excellent electro-optical properties. Therefore, it is widely used in electro-optic modulators (Haretling, 1999; Dimos, 1995), and optical displays (Uchino, 1995; Moulson and Herbert, 1997). With the rapid development of optical telecommunications and optical networks, the electro-optical applications of PLZT materials are becoming more and more important. For these applications, it is essential to grow a highly oriented or epitaxial microstructure in order to reduce optical loss, which is mainly caused by light scattering at grain boundaries because of the inhomogeneous refractive indices. Thus the synthesis and processing of epitaxial PLZT thin films have been investigated intensively.

In *n*Gimat, PLZT thin films with various La contents and Zr to Ti ratios have been grown epitaxially on *c*-sapphire substrate with an epitaxial $Pb_{1-x}La_xTiO_3$ (PLT) seed layer. As known, Sapphire has a different crystal structure than $LaAlO_3$ (LAO) and MgO, which have cubic structure and are common substrates for PLZT thin films. The lattice mismatch between PLZT and sapphire is much larger than those between PLZT and LAO or MgO. A PLT seed layer with cubic structure can promote the epitaxial growth of PLZT films on sapphire substrates. Figure 7 shows the XRD patterns, which were created by ***Chi*** integration along the substrate normal from area detector XRD patterns, of PLZT thin films with various La contents and Zr to Ti ratios on *c*-sapphire substrate. It is clear that the XRD patterns of the PLZT 20/30/70, PLZT 17/40/60, and PLZT 17/50/50 thin films show only (111) peaks, indicating that these films inherited the epitaxy of PLT seed layer and were grown epitaxially on *c*-sapphire substrate with (111) plane parallel to the substrate surface. However, the XRD pattern of the PLZT 15/30/70 film shows small extra peaks of (100) and (110), and those of the PLZT 12/40/60 and PLZT 15/50/50 films show extra (110) peaks, suggesting that these films were grown preferentially with multi-orientations parallel to the substrate surface. Further studies showed that for PLZT films with a Zr to Ti ratio of 30:70, 40:60, and 50:50, when La content is lower than 20, 17, and 16 mol.%, respectively, the PLZT film grew preferentially with multiple out-of-plane orientations with or without randomly oriented grains in plane, which depends on the composition. According to the PLZT phase diagram (Haertling and Land, 1971), for PLZT materials with a Zr to Ti ratio of 30:70, 40:60, and 50:50, when La content is lower than about 20, 17, and 16 mol.%, respectively, the crystal structure is tetragonal. Therefore, the large lattice mismatch between PLZT and *c*-sapphire limits the epitaxial growth of PLZT thin films with these compositions on *c*-sapphire substrate. However, the PLZT films with these compositions can be grown epitaxially on $SrTiO_3$ (100) or *r*-sapphire with (100) or (110) plane parallel to the substrate surface, respectively (Yoon et al., 1994).

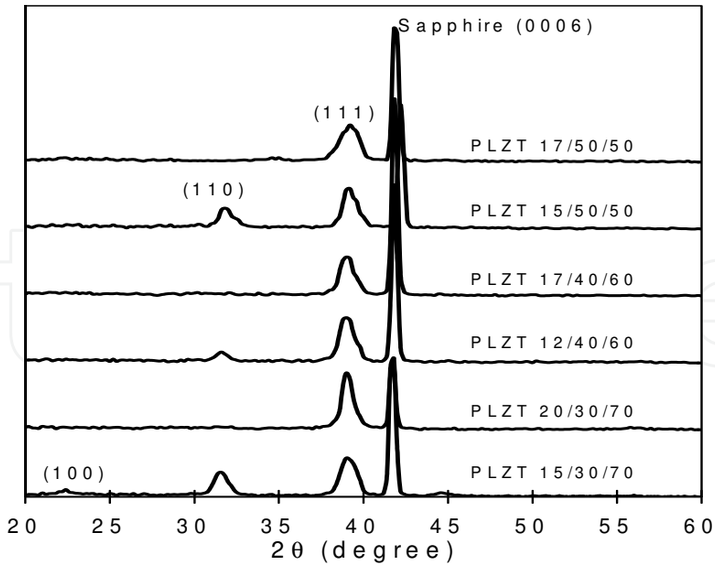

Fig. 7. XRD patterns of the PLZT thin films with various La contents and Zr to Ti ratios by CCVD on *c*-sapphire substrate with a PLT seed layer

Pole figure measurements were performed on the epitaxial films using (110) reflections. The pole figure of a PLZT 20/30/70 thin film is shown in Figure 8. As BST thin films on *c*-sapphire, the PLZT thin film shows six sharp dots of (110) poles with narrow density distributions, which is similar to that of the PLT seed layer. There is no broadening or satellite found from the pole figure, suggesting an excellent crystallinity. The PLZT films grew off the PLT seed layer and keep the crystallographic orientations. The orientation relationship between the PLZT thin film and *c*-sapphire substrate is PLZT (111)//sapphire (001) and PLZT [110]//sapphire [104].

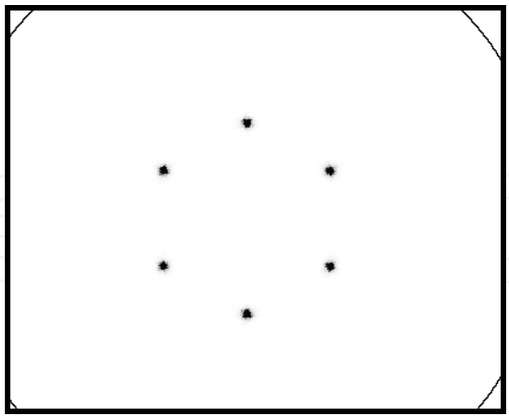

Fig. 8. (110) pole figure of a PLZT 20/30/70 thin film on *c*-sapphire substrate with a PLT seed layer

Figure 9 shows the SEM micrographs of the PLZT thin films with different compositions. These PLZT thin films inherit the microstructure of the PLT seed layer. They contain uniformly distributed fine grains less than 100 nm in size. The film morphology is strongly influenced by the film composition. For the film with a Zr to Ti ratio of 50/50 (not shown in

the figure), the grains are not closely packed. Voids and pores were formed in this film. With the increase of Ti content and the decrease of Zr content, the film density increases and the grain size decreases. For the film PLZT 20/30/70, there is no pin hole formed. All of these films are crack free. It is also noticed that particles were formed on these films, which may be attributed to poor atomization or high flame temperature. Further studies show that without the PLT seed layer the PLZT films deposited at the same conditions contain multiple out-of-plane orientations or are random. Pyrochlore phase was also formed at these conditions for variety of compositions without a PLT seed layer. Therefore, the PLT seed layer can markedly enhance the formation kinetics of perovskite phase and improve the crystallization behavior of the PLZT thin films subsequently deposited. The probable cause for the presence of pyrochlore phase is that the lattice mismatch between the sapphire substrate and PLZT thin films hinders the phase transformation process (Kao et al., 2003).

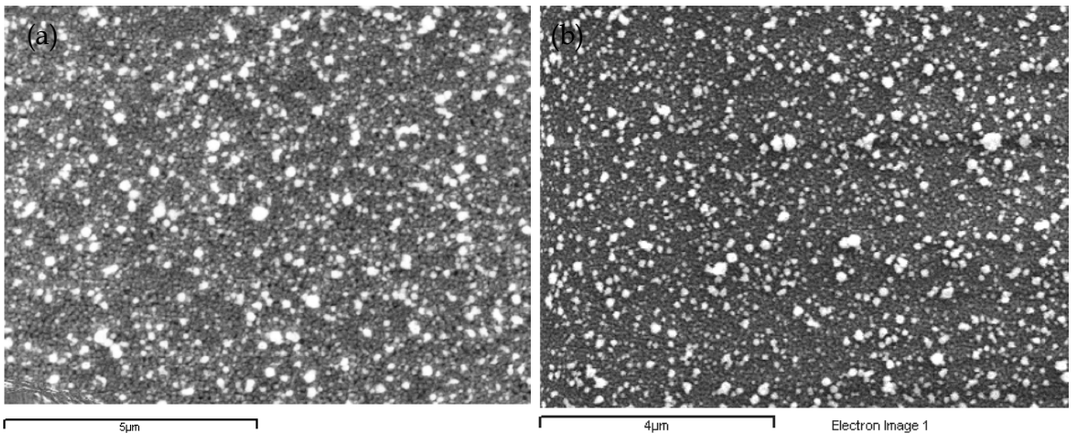

Fig. 9. SEM images of PLZT thin films with different La contents and Zr to Ti ratios on *c*-sapphire substrates with a PLT seed layer, (a) PLZT 17/40/60 and (b) PLZT 20/30/70

The optical properties of these PLZT thin films were measured by a spectrometer in the visible and near infrared regions. For composition, all the transmittance was normalized to the sapphire substrate. As shown in Figure 10, it is found that all the three films have a transmittance of higher than 70% and 90% in the visible region and near infrared region, respectively. High transmittance is necessary for optical applications such as optical modulators and switches. The waveguiding modes and refractive indices of these thin films will be measured by a prism coupler later.

3.3 Depositions of CCT thin films by CCVD and their properties

In recent years, $CaCu_3Ti_4O_{12}$ (CCT) has been attracting much attention due to its extraordinary high dielectric constant of about 10^5 at room temperature and very small temperature dependence of the dielectric constant over a wide temperature range from 100 to 600 K (Subramanian et al., 2000, 2002; Ramirez et al, 2000; Home et al., 2001; Adams, et al., 2002; Sinclair et al., 2002; Maurya, et al. 2008; Prakash, et al., 2008; Zhu, et al., 2008; Kim, et al., 2010). CCT and its family, $ACu_3Ti_4O_{12}$ (A = rare earth or other alkali earth element), were first identified in 1967 (Deschavnres et al., 1967). Since then, this family has been expanded. Its accurate structure was determined in 1979 (Bochu et al., 1979). CCT has a body-centered cubic structure with a centro-symmetric space group *Im3* and two formula units per unit

cell. Its cubic structure is related to that of perovskite ($CaTiO_3$), but the TiO_6 octahedra are tilted to produce a square planar environment for Cu^{2+}. Cu atoms are bonded to the four oxygen atoms and the large Ca atoms are without bonds.

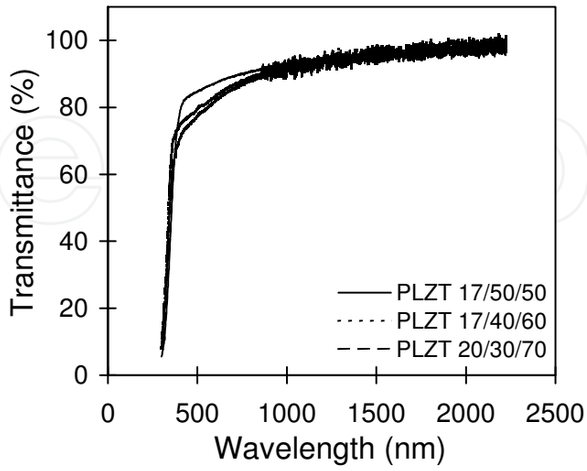

Fig. 10. Optical transmittance spectra of PLZT thin films with various La contents and Zr to Ti ratios grown on *c*-sapphire substrate with a PLT seed layer

Subramanian and coworkers (Subramanian et al., 2000, 2002) prepared CCT based ceramics by sintering related powders. A dielectric constant of higher than 10^5 was achieved at room temperature. The dielectric constant increases rapidly with the increase of temperature and reaches 3×10^5 at 450°C. Based on Subramanian's work, Ramirez and coworkers (Ramirez, et al., 2000) extended the measurement temperature range to cryogenic values and additional measurements were performed on the CCT compound. Dielectric measurements showed that over the temperature range of 100-380 K, ε_r is higher than 10000 and only weakly temperature dependent at 1 kHz.

While its extraordinary dielectric constant has generated huge interest, the origin of the high dielectric constant and its sharp decrease at 100 and 600 K has also attracted intensive studies. Many studies argue against an explanation in terms of ferroelectricity since there has been no phase or structure transition observed. Several other intrinsic physical mechanisms suggested include high tension on Ti-O bonds (Subramanian, et al., 2000), highly polarizable relaxational modes (Ramirez, et al., 2000), and a relaxor-like dynamical slowing down of dipolar fluctuations in nanosize domains (Home, et al., 2001). However, it was also suggested that the giant dielectric constant of this material may be enhanced by its microstructure such as the barrier layer mechanism (Subramanian, et al., 2000; Adams, et al., 2002; Sinclair, et al., 2002; Li, et al., 2009). In their studies, impedance spectroscopy measurements show that CCT ceramics are electrically inhomogeneous, contains semiconducting grains with insulating grain boundaries that is the desired electrical microstructure for internal barrier layer capacitors (BLC).

Although excellent electrical properties have been achieved on CCT bulk ceramics, for microelectronic applications, thin films are preferred since thin films can provide a higher level of integration than can be achieved with discrete components by bulk materials, and hence the devices are faster, lighter, and of lower cost. Furthermore, single-layer, thin-film devices intrinsically have lower inductance than multilayer capacitors because of the high

mutual inductance between the internal counter electrodes (Dimos and Mueller, 1998). *n*Gimat has successfully deposited CCT thin films on various single crystal substrates, including single crystal STO, single crystal $LaAlO_3$ (100), *c*-sapphire, and *r*-sapphire, by its proprietary CCVD process. Materials and electrical properties were characterized.

3.3.1 CCT thin films on STO substrate

CCT has a body-centered-cubic structure with a lattice parameter, *a*, of 7.393 Å. STO has a cubic perovskite structure with a lattice constant of 3.905 Å. STO single crystal is one of the most popular substrates for high temperature superconductors and other electronic materials because of its high thermal and chemical stabilities and compatible lattice constant and structure. In this study, stoichiometric CCT thin films with different thickness were first grown on STO (100) substrates between 950 and 1025°C. The XRD spectra integrated along the substrate normal direction from the area detector XRD patterns are shown in Figure 11. It is clear that the main peak of these films is CCT (400) which aligns well with STO (200) diffraction, suggesting a highly (*l*00) preferred growth of the CCT films. There is a small (220) peak for all these films, implying a little portion of random or mis-oriented grains with (220) plane parallel to the substrate surface. Dielectric constant as a function of film thickness is shown in Figure 12. The dielectric constant of the CCT films on STO substrates decreases with the increase of film thickness. At a thickness of 45 nm, which was deposited at 950°C for 10 min, the dielectric constant is about 45,000, while at a thickness of 400 nm, which as deposited at 1025°C for 40 min, the dielectric constant is about 5,900. The dielectric constant is approximately proportional to the reciprocal of film thickness based on the simulation of the data points. The lower dielectric constant of the thicker films deposited at higher temperatures could also be caused by the higher stress between the CCT film and the substrate, which needs to be further understood.

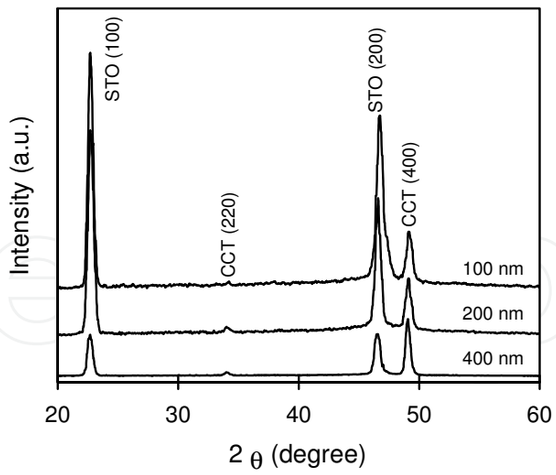

Fig. 11. XRD spectra of CCT thin films deposited at 1025°C on STO substrate with different thickness

The frequency and bias voltage dependence of dielectric constant and quality factor of a 45 nm thick CCT film on STO substrates are shown in Figure 13. In the tested frequency range, dielectric constant decreases slightly while quality factor increases with the increase of bias voltage. For example, at 1 MHz and 0 V, the dielectric constant and quality factor are 45,320

and 730, respectively. When applying a bias voltage of 40 V, at the same frequency, the dielectric constant and quality became 44,950 and 950, respectively. In tested voltage range, when frequency is lower than 1 MHz, dielectric constant decreases gradually with the increasing of frequency. It shows a sharp decrease at the frequency of 10 MHz at all the tested voltages. However, quality factor increases rapidly with the increase of frequency in the tested voltage range.

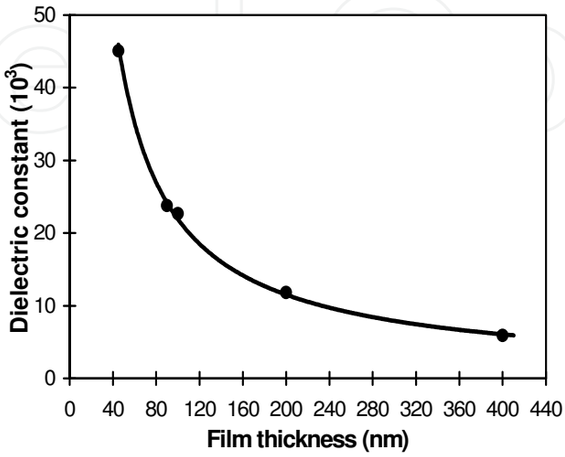

Fig. 12. Dielectric constant of CCT films on STO (100) substrates as a function of film thickness

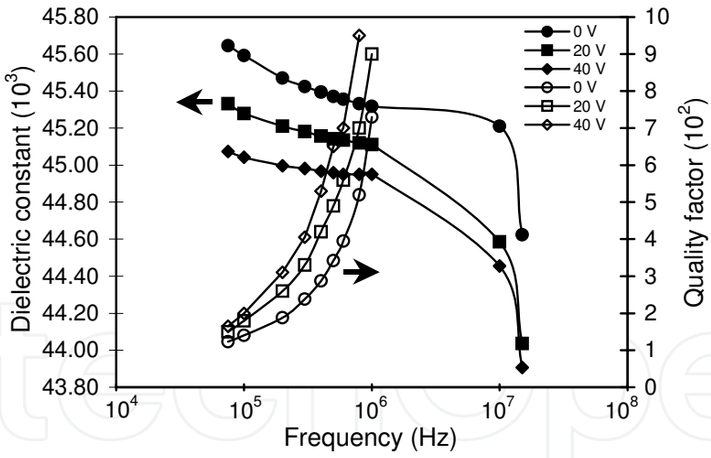

Fig. 13. Dielectric constant and quality factor of a CCT film, deposited at 950°C for 10 min on STO (100) substrate, as a function of frequency at different bias voltages

3.3.2 CCT thin films on *c*-sapphire substrate

Sapphire (α-Al_2O_3) has a hexagonal crystal structure with a = 4.759 Å and c = 12.99 Å. It is widely used to deposit ferroelectric materials for electrooptic applications and radiation hardened electronic components. Sapphire has a different crystal structure than LAO or STO. Also, the lattice mismatch between CCT and sapphire is much larger than those between CCT and LAO or STO. Therefore, the growth of CCT on sapphire is different from that of CCT on LAO or STO. Stoichiometric CCT films with different thickness were

deposited onto *c*-sapphire at a temperature of 1025°C. Figure 14 (a) shows the SEM image of a 90 nm thick CCT film. The base layer of the film is dense and smooth with uniform and fine grains. There are a few hillocks on its surface. With the increase of film thickness, the films become rougher and grains become larger. The area detector XRD patterns show preferred growth of these CCT films with multiple orientations, including (220), (222), and (400), which is consistent with the corresponding morphology with square and pyramid shaped grains stacking on each other that can be seen clearly in the thicker films. This is confirmed by the integrated XRD spectra along the substrate normal, shown in Figure 14 (b), which match the characteristics of the CCT compound. There are also some in-plane and out-of-plane random grains formed in these films. It is noticed that (310) and (321) diffractions became stronger with the increase of film thickness as well.

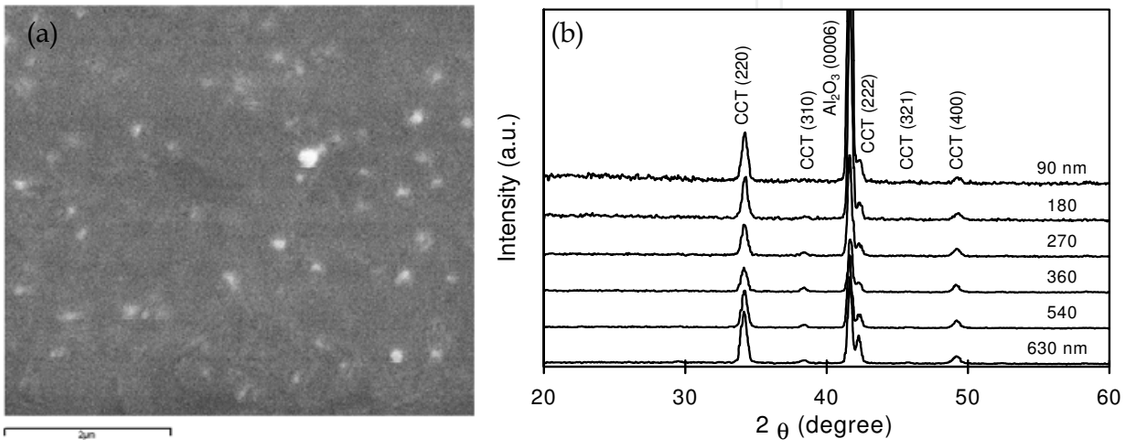

Fig. 14. (a) SEM image of a 90 nm thick CCT film and (b) XRD spectra of CCT films with different thickness

The dielectric constant of CCT films on *c*-sapphire substrates, as shown in Figure 15, decreases with the increase of film thickness, which is similar to those of CCT on STO and LAO, but with lower values. The dielectric constant is about 930 for a 90 nm thick film. It decreases to about 235 when film thickness increases to 630 nm.

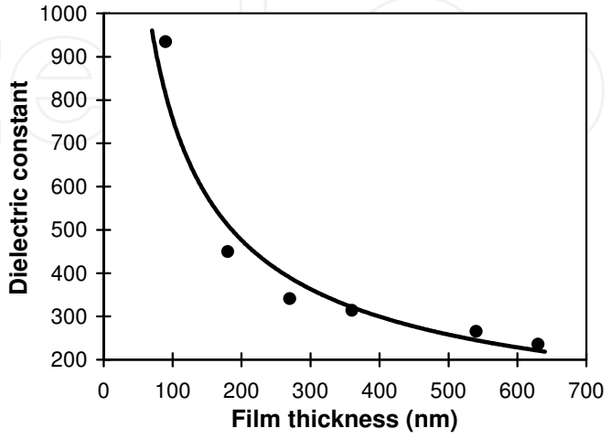

Fig. 15. Dielectric constant of CCT films on *c*-sapphire substrates as a function of film thickness

From the results of CCT films on different substrates, it is clear that CCT films on STO have the highest dielectric constant while the ones on c-sapphire substrates have the lowest. It is worthwhile to point out that the observation of the dielectric constant decreasing with increasing film thickness in this study is contrast to the fact found in other ferroelectric thin films such as $Ba_xSr_{1-x}TiO_3$ (BST) and CCT on platnized Si wafers. Conventionally the dielectric collapse is understood by assuming the existence of "dead layers" with severely depressed dielectric constants at the electrode-dielectric interfaces. These dead layers act as parasitic capacitors in series with the "bulk-like" dielectrics. Hence the decrease in dielectric constant is said to follow the "series capacitor model" (Sinnamon et al., 2002). Various suggestions on the exact nature of the dead layers, although still under debate, have been proposed in these years (Sinnamon et al., 2002; Streiffer et al., 1999), including (1) the interfacial discontinuity affecting the polarization states in the dielectric close to the electrode-dielectric interface (Zhou and Newns, 1997; Natori et al., 1998; as cited in Sinnamon et al., 2002), (2) Schottky barriers formed as a result of mis-match in the band structure between dielectric and electrode (Hwang et al., 1999; Scott, 1999; as cited in Sinnamon et al., 2002), and (3) thickness-related soft-mode hardening (Sirenko et al., 2000, as cited in Sinnamon et al., 2002). The different phenomenon observed in this study could be attributed to different residual stress states, and orientations, etc.

For comparison, Table 3 summarizes the results for all the substrates studied with approximately the same CCT film thickness. For bulk CCT materials, the peak intensity ratio of (220), (222), and (400) is 100:30:80. Therefore, CCT films on STO and LAO substrates are highly (400) preferred while CCT films on sapphire substrates are (220) preferred.

Substrate	Thickness (nm)	Orientation (Intensity ratio)	Dielectric constant
STO (100)	200	(220) + (400) (100:746)	11825
LAO (100)	180	(220) + (400) (100:892)	1188
c-Sapphire	180	(220) + (222) + (400) (100:42:19)	450

Table 3. Comparison between substrates, film thickness, orientation, and dielectric constant

4. Applications of BST based thin films

Telecommunications require the use of filters throughout RF devices. For high frequency receivers, filters must be used to remove signals in unwanted frequency bands to prevent overload of the receiver itself and undesirable interference from signals outside the band of operation. On the transmit side, signal purity must be maintained to minimize interference to other users and the incoming signal, conform with government regulations for radio emissions, and in the case of military applications to minimize detection of the radio source by hostile forces. Current technology in both the commercial and military fields employs ceramic blocks or quartz substrates and complex metallization patterns to define the filter response. The resulting filter structures operate on a narrow set of frequencies, determined at the time of device fabrication. A radar or communications device capable of operating on multiple frequency bands requires complex and expensive banks of filters connected with microwave switches or PIN diodes.

In addition, currently wireless communications can readily be monitored or jammed. Different agencies can't directly contact each other due to assigned specific frequencies. Instead of traditional fixed frequency filters set for specific bands, a new generation of

rapidly variable filters will be available to provide tactical capability. These existing issues can be overcome through reconfiguring transmission and reception in a few microseconds using tunable filters. Low cost, low loss, high IIP_3, high speed, robust, and radiation-hard filters can enable wide adaptations. Planar low-voltage capacitor structures with improved power handling capability have been developed using BST films and used in the design and fabrication of tunable filters operated at frequencies of 2, 6-20, and 30-45 GHz. In the past several years, *n*Gimat has worked on materials development, as well as design, fabrication, and testing of tunable ferroelectric thin film based microwave devices.

4.1 RF MEMS filters with tunable bandwidth and tunable center frequency

For this application, a CPW admittance inverter topology was employed to realize a Ka-band tunable filter. Two configurations, wideband (WB) and narrowband (NB), were designed, as shown in Figure 16. The electronic realization of bandwidth control is accomplished by introducing a ground-to-ground connection through the inter-resonator gaps as shown in Figure 16 (b). For proof-of concept, perfect open and short connections were used at first. Figure 17 shows the measured results of wideband and narrowband 3-pole filters without BST capacitors. Their bandwidths are 4% and 8% respectively, with a center frequency of 39.5 GHz.

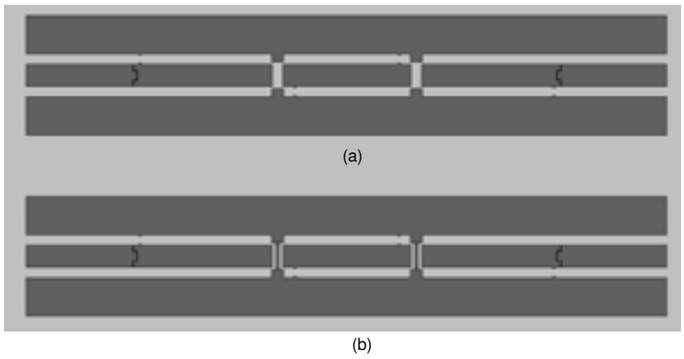

Fig. 16. 3-pole filter topologies: (a) wideband and (b) narrowband configuration

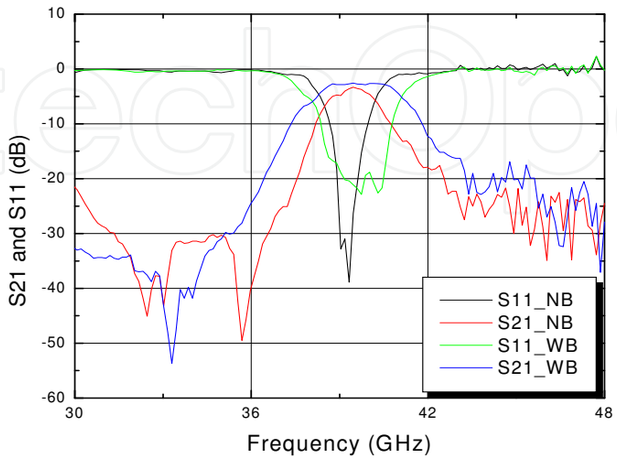

Fig. 17. Measured S parameters of 3-pole wideband and narrowband filters (no BST capacitors)

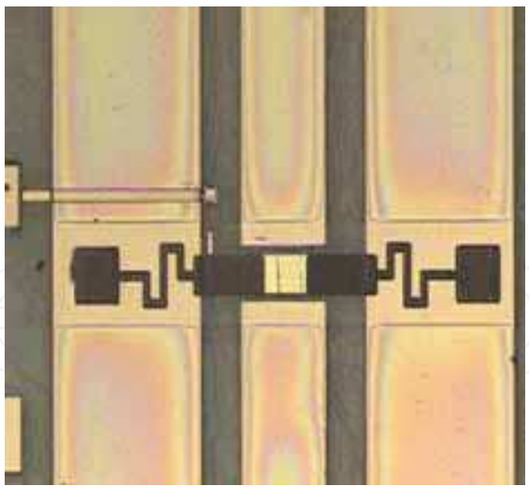

Fig. 18. A 2-pole CPW admittance inverter tunable filter with MEMS switches

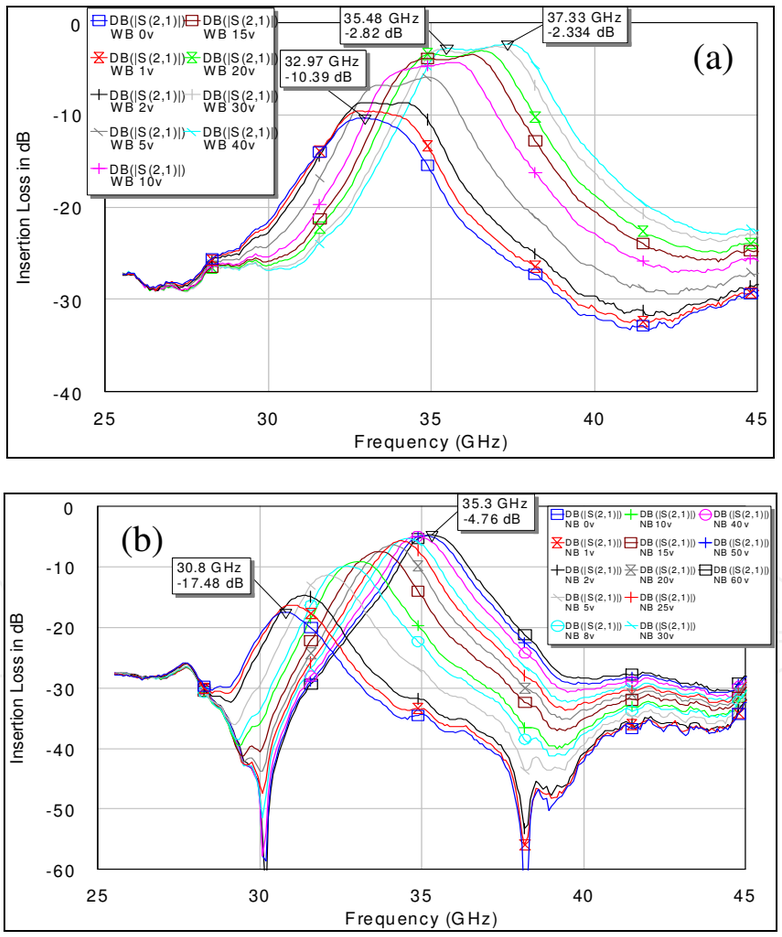

Fig. 19. Measured insertion loss, S_{21}, of a 2-pole CPW admittance inverter filter with MEMS switches (a) at the up and (b) at the down state, each curve representing the insertion loss at one voltage level

RF microelectromechanical systems (MEMS) filters were also designed and fabricated, as shown in Figure 18. Two MEMS switches are used to realize ground-to-ground connection. One bias pad is used to activate the switches. When the MEMS are at the up state, the filter is wideband. A narrowband filter results when the switches are at the down state. The RF MEMS filter was tested up to 45 GHz. Figure 19 (a) presents the insertion loss of the filter. The filter has an insertion loss, S_{21}, of 10.4 dB, a return loss, S_{11}, of ~5 dB, and a bandwidth of 8.3 % at 0 V. The S_{21} and S_{11} are <3 dB and ~10 dB, respectively, when the BST capacitors are biased at 40 V. The center frequency moves >3 GHz (10% tunability). When the MEMS switches are at the down state (narrowband), as shown in Figure 19 (b), the filter has an S_{21} of 17.5 dB, a S_{11} of ~5.3 dB, and a bandwidth of 5 % at 0 V. The S_{21} and S_{11} are <4.8 dB and 17 dB respectively when the BST capacitors are biased to 60 V. The center frequency moves from 30.8 to 35.3 GHz (13.6% tunability). To the best of our knowledge, this is the first time that a BST tunable filter has ever been realized at the mm-wave frequency with such performance.

4.2 CDMA tunable filters operated at the 1.9 GHz band

Code Division Multiple Access (CDMA) is one of the digital cellular technologies deployed worldwide. A prototype 2-pole, 1-zero frequency-agile band-pass CDMA Tx filter was designed and fabricated, as shown in Figure 20 (a). A 2-resonator ceramic block with a BST tunable device fabricated by standard IC technique is used to tune the filter's center frequency. Table 4 shows typical specifications of a US personal communication service (PCS) antenna duplexer. In order to meet these stringent specifications, the fixed-tuned ceramic filters on today's cellular market typically have 6 poles on the receive and 5 on the transmit side. They can be significantly simplified using the tunable filters, which results in smaller physical size and lower insertion loss. Figure 20 (b) shows the CDMA filter response. An insertion loss of 2.0 dB or less and a tuning of required 60 MHz are achieved at a DC bias of 10 V.

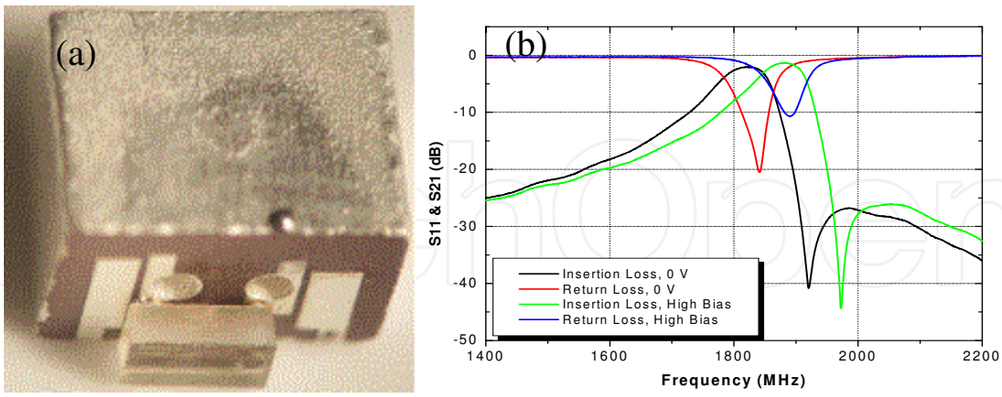

Fig. 20. (a) CDMA filter prototype, (b) CDMA Filter Response at 0V and high DC bias

4.3 X-band to Ku-band tunable filters

Slow wave resonators (SWR) are sections of transmission lines periodically loaded with tunable BST capacitors. By changing simultaneously the capacitance of each BST device, the effective dielectric constant, thus, the electrical length of the resonator is changed so that a different resonance frequency is achieved. In addition, due to the increased effective

Parameter	Values
Tx to antenna frequency fange	1850 – 1910 MHz
Insertion loss	2 dB max.
Return loss	12 dB
Attenuation at Rx	40 dB
Antenna to Rx frequency range	1930 – 1990 MHz
Insertion loss	2.0 dB max
Return loss	12 dB
Attenuation at Tx	45 dB
Tx to Rx isolation	
1850-1910	50 dB
1930-1990	40 dB

Table 4. Typical specifications of a US PCS duplexer

dielectric constant the resulting filters are more compact (smaller size) when compared to the regular resonator ($\lambda/2$ or $\lambda/4$) filters. The change in the effective dielectric constant also results in a characteristic impedance change.

A prototype of a 3-pole SWR filter with a dimension of 8.30 mm × 2.65 mm is shown in Figure 21. Figure 22 shows the microwave results of a 2-pole and a 3-pole SWR filter. Both filters have the same tuning range, i.e. 4.15 GHz, which corresponds to a tunability of 48%. The 3-pole filter shows higher loss due to its narrower bandwidth and possibly more capacitors, but has much better stop-band rejection than the 2-pole one. Proprietary low voltage electrode (LVE) BST capacitors were also used in the filter design, replacing regular gap capacitors. Figure 23 shows the measured S_{21} and S_{11} of a 2-pole low-voltage SWR filter. The filter shows an S_{21} of 5.4 and 3.3 dB at 0 and 30 V, respectively. The S_{11} is greater than 10 dB. The 3-dB bandwidth is between 14-15% at all bias voltages. The center frequency at 0 V is 11.5 GHz. The tunability is about 2.3 GHz (20% tuning).

Fig. 21. A prototype of a 3-pole SWR filter with a total of 8 DC blocking capacitors

4.4 X-band back-to-back 4-pole band-pass filters

A tunable back-to-back 4-pole filter was built on a flexible organic liquid crystal polymer (LCP) substrate, which consists of two open-loop resonators coupled to the two others through apertures lithographically opened in their common ground plane, resulting in a footprint size reduction of about 50% compared to typical open-loop resonator based filters. The filter frequency is tuned using BST capacitor chips, which are mounted and ribbon-bonded between both ends of each resonator on both sides. An insertion loss of 1.8 - 5.4 dB and a tuning of 12.6% are achieved in frequency range of 9.3 – 10.1 GHz.

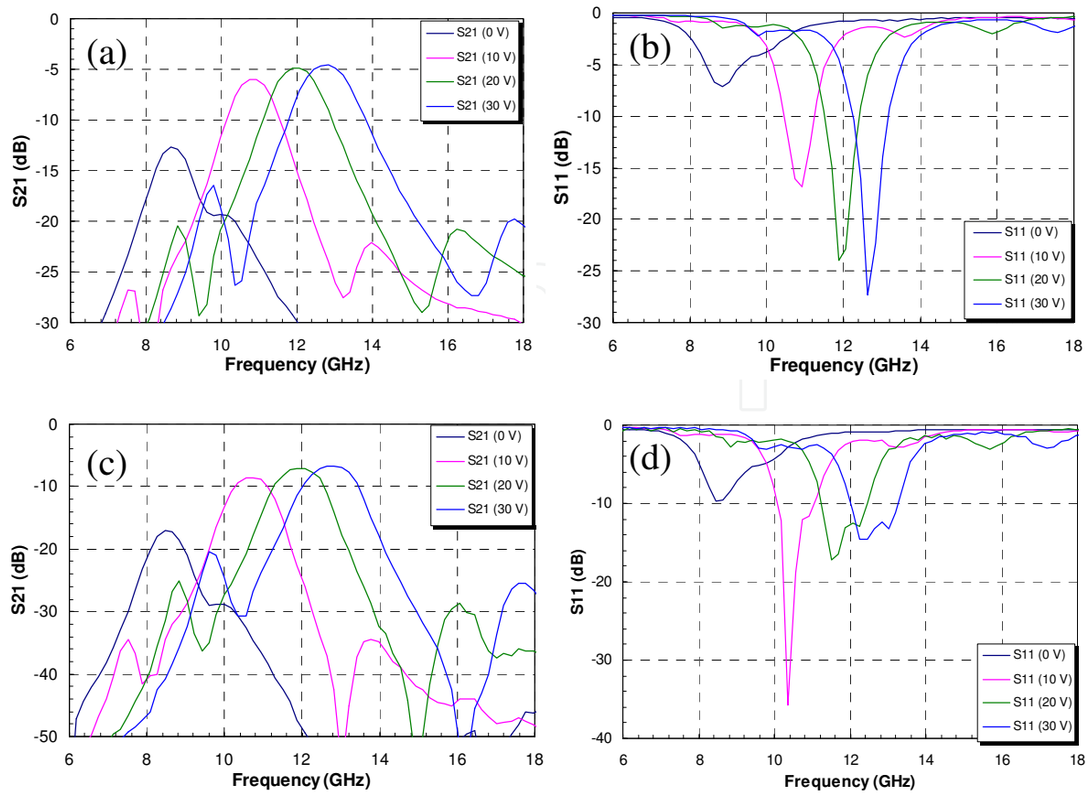

Fig. 22. Measured (a) insertion loss and (b) return loss of a 2-pole and (c) insertion loss and (d) return loss of a 3-pole SWR filter

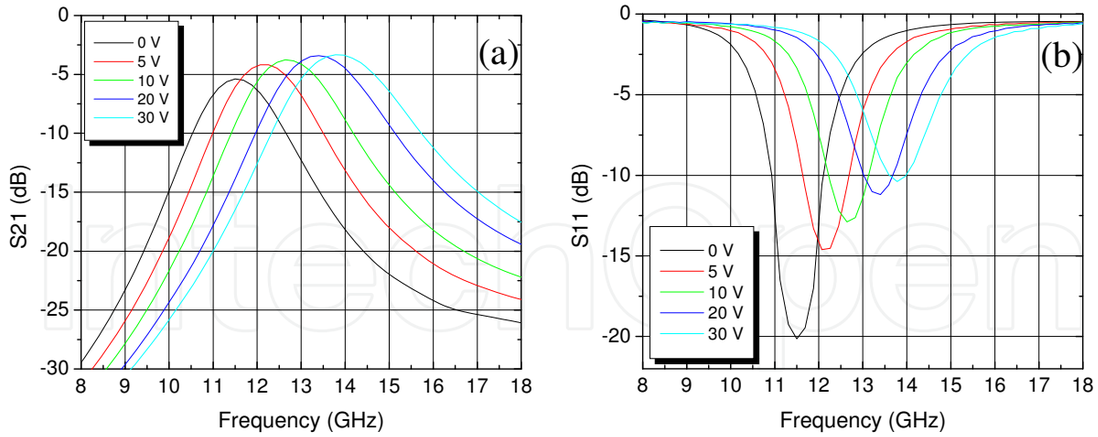

Fig. 23. Measured (a) insertion and (b) return loss (SOLT cal) of a 2-pole low-voltage SWR filter using LVE BST capacitors

The fabrication requires two 200 µm thick LCP layers originally covered by a 9 µm Cu foil. The top resonators (1 and 4) are patterned on one side of the first layer while the coupling apertures are patterned on the other side using conventional lithography techniques. As for the second layer, Cu is completely etched off on one side while bottom resonators (2 and 3) are patterned on the other side. A 25 µm LCP bond ply layer is placed between both layers

which are aligned and bonded together with a substrate bonder at a temperature of 280 °C. The BST capacitor chips are then mounted on both sides and ribbon-bonded to the resonators. A 75 µm wide ribbon bond is used in order to limit the induced series inductance. High resistors are also surface mounted on the bottom layer to isolate the RF signal from the bias network. A photograph of both sides of the fabricated filter including the bias network is shown in Figure 24.

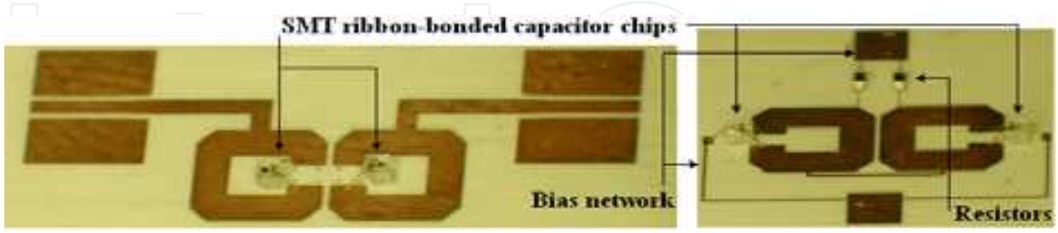

Fig. 24. Prototype of the 4-pole tunable filter with mounted capacitors: oblique views of the (a) top resonators (1 and 4) and (b) bottom resonators (2 and 3)

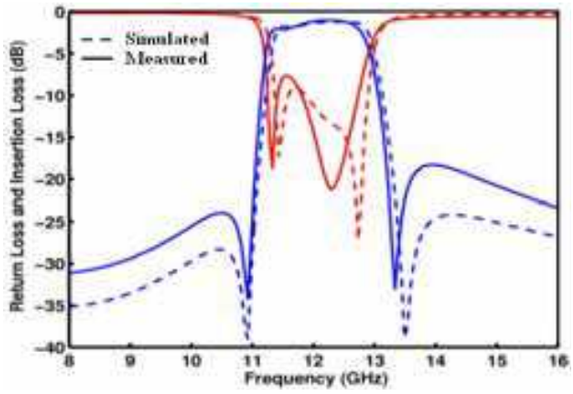

Fig. 25. Measured filter response without capacitors, compared to the simulated response

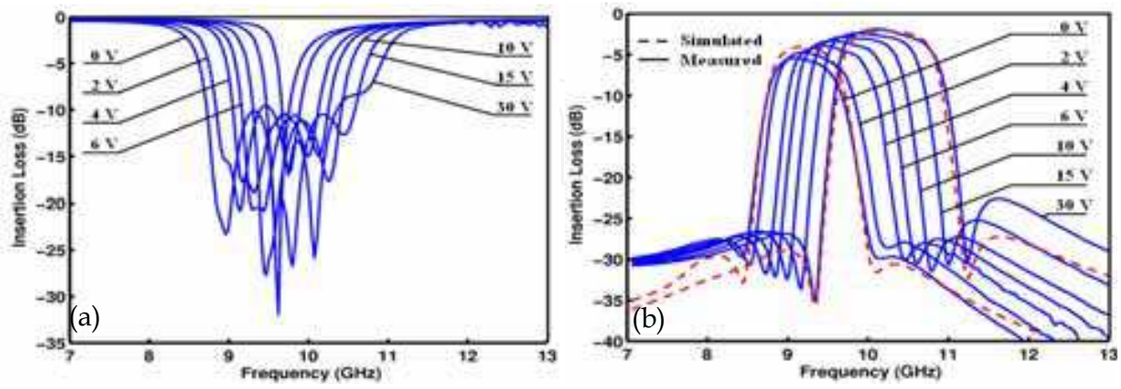

Fig. 26. Measured (a) return and (b) insertion loss of the 4-pole tunable filter

Figure 25 presents measured return and insertion loss of the filter compared to simulated results, showing a good agreement. Measured insertion loss is 1.0 dB at 12.23 GHz with a bandwidth of 11.2% at 1 dB. The measurement includes the via-less coplanar-to-microstrip

transition effects which are not de-embedded. BST capacitors are then mounted on the substrate and ribbon-bonded. A bias voltage of 0 to 30 V is applied to the four capacitors to tune the center frequency. Figure 26 presents the measured results. The measured insertion loss is also compared to the simulated ones with a serial resistance of 6 Ω, an inductance of 0.6 nH, and a capacitance of 90 fF at 0 V and 54 fF at 30 V. An insertion loss of 5.4 dB at 9.1 GHz and 1.84 dB at 10.25 GHz is achieved, resulting in an analog tuning of 12.6% with a capacitance ratio of 1.67:1. Return loss is lower than 10 dB over the whole frequency range.

4.5 Ka-band ring tunable filters

Ka-band ring tunable filters with a size of 4.73 × 3.5 mm have also been fabricated on the BST based films, as shown in Figure 27. Each resonator consists of a ring separated by a thin gap, C_{gap}, from a stub protruding from a microstrip. The resonant frequency of each ring is tuned by the BST capacitors between the rings and ground. Radial stubs are used to realize electrical short to the RF ground, simplifying the fabrication process by eliminating via drilling through sapphire. Figure 28 shows the tuning of the fabricated filter. The best

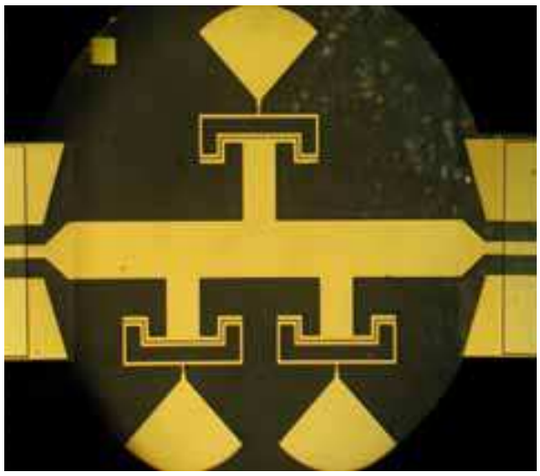

Fig. 27. Photograph of a ring filter

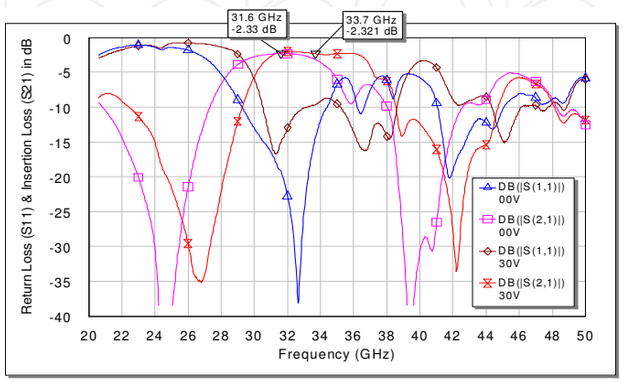

Fig. 28. Measured S-parameters for Ka-band ring filter under different biases (blue=S_{11} and pink=S_{21} at 0V; brown=S_{11} and red=S_{21} at 30 V

insertion loss in pass-band is 2.3 and 2.0 dB at 0 and 30 V, respectively. The 3-dB bandwidth is 20% for both bias states. The filter tunes from 31.6 to 33.7 GHz, a 6.6% tunability.

4.6 Phase shifters

In the meanwhile, phase shifters have also been developed using ferroelectric BST capacitors for frequencies ranging from L- to Ka-band. The all pass network shown in Figure 29 is realized using tunable BST capacitors and planar inductor structures. The resulting phase shifters exhibit low loss and phase shift greater than 360° using a low bias voltage. The main advantages of these phase shifters include small size, full passivation to prevent failure from contaminations, no static power consumption, solder ball termination for direct flip-chip mounting on a carrier, coplanar waveguide input and output to facilitate transition to other circuitry, and lumped element design for low loss. Figure 30 shows the insertion S_{21} and S_{11} of a 3 GHz phase shifter with a dimension of 2.46 × 1.83 × 0.44 mm developed at *n*Gimat. The maximum insertion loss at 3 GHz is 4.3 dB at 15 V. The figure of merit is 89.4°/dB at 0V and 89.2°/dB when the measurements at 0, 5, 10, 15, 20, 25, 30, and 35V are averaged. The S_{11}, shown in Figure 30 (b), is lower than 11.5 dB in all biased states. A phase shift of 376° is measured at 35V as shown in Figure 31. Another example of *n*Gimat's Ka-band phase shifter is discussed by Courrèges, et al (Courrèges et al., 2010). At 36 GHz, the phase shifter has the maximum S_{21} of 6.8 dB at 0V. The S_{11} is <10 dB in all biased states. A phase shift of 361° is measured at 30 V.

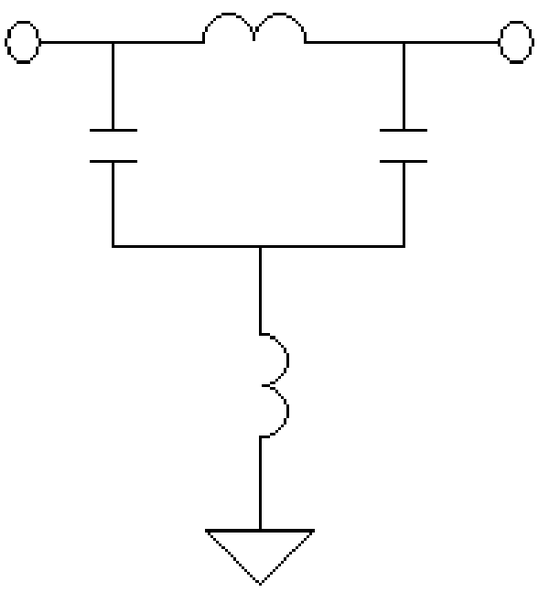

Fig. 29. Schematic of all-pass network

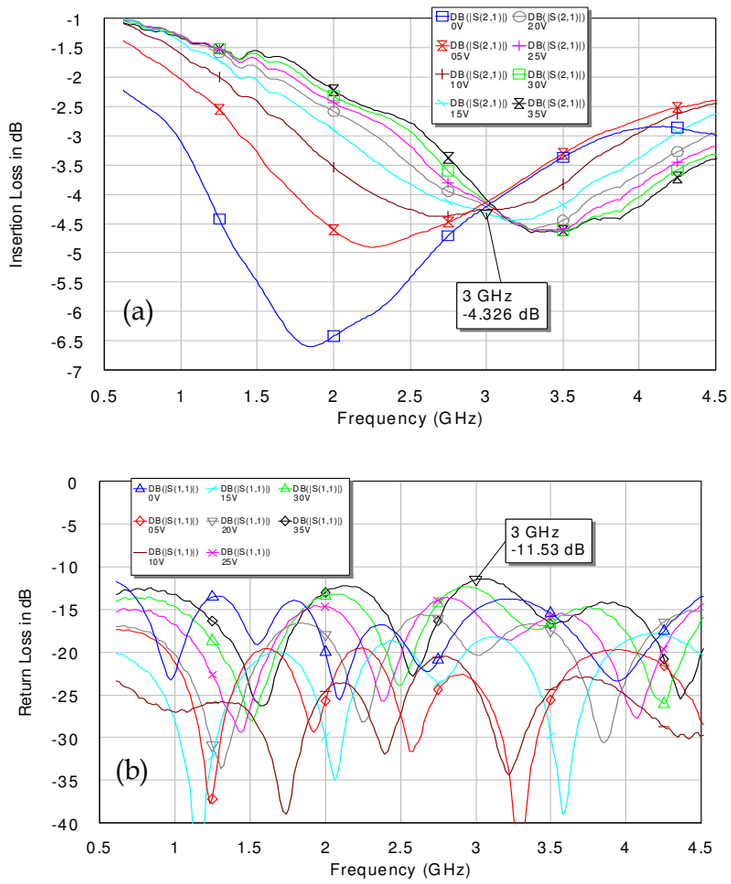

Fig. 30. (a) Insertion loss, S21 and (b) return loss, S11 of 3 GHz phase shifter

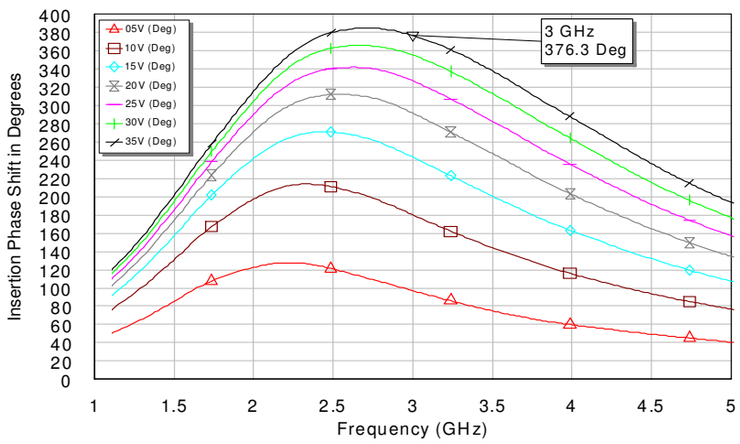

Fig. 31. Phase shift of the 3 GHz phase shifter at different frequencies and bias voltages

5. Conclusions

As a summary, high quality epitaxial or textured ferroelectric and dielectric thin films, including BST (both single layer and nanostructured multilayer), PZT, and CCT, have been successfully deposited by the proprietary CCVD process onto various substrates, including sapphire and single crystal STO, MgO, and LAO etc. Excellent electrical properties have been achieved on these ferroelectric and dielectric thin films. High performance microwave devices that can be used up to Ka band, such as tunable MEMS filters and CDMA filters, have been designed and fabricated on BST based ferroelectric thin films. The performance of these microwave devices are summarized as following:

- MEMS Ka-band tunable bandpass filters (both center frequency and bandwidth are tunable): the best insertion loss of 3 dB when biased, and the bandwidths of 3 and 7.8% for 3-pole narrowband and wideband, respectively;
- CDMA Tx tunable filters: insertion loss <2 dB, VSWR <1.5:1, center frequency shifting from 1.85 to 1.91 GHz, Rx zero (@1.93 GHz) rejection >40 dB, DC bias <10 V;
- X- to Ku-band tunable bandpass filters: insertion loss of ~5 dB @11.5 GHz (0V) to 3 dB @14 GHz (30 V), VSWR <2:1, DC bias <30 V, 6 × 1.5 × 0.5 mm in footprint;
- X-band back-to-back 4-pole bandpass filters: Insertion loss from 5.4 dB at 9.1 GHz to 1.84 dB at 10.25 GHz with an analog tuning of 12.6%; return loss <10 dB over the whole X-band frequency range;
- Ka-band ring filters: insertion loss of 2.3 and 2.0 dB for 0 and 30 V, respectively; 3-dB bandwidth of 20% for both bias states; tuning from 31.6 to 33.7 GHz, a 6.3% tunability;
- 3 GHz phase shifter: The insertion loss at is 4.3 dB at 15 V and 3 GHz. The figure of merit is 89.4°/dB at 0V. A phase shift of 361° is measured at 30V.

6. References

Adams, T. B., Sinclair, D. C., and West, A. R. (2002). Giant Barrier Layer Capacitance Effects in $CaCu_3Ti_4O_{12}$ Ceramics. *Advanced Materials*, Vol.14, No.18, (Sept 2002), pp. 1321-1323, ISSN 1521-4095

Bao, P., Jackson, T. J., Wang, X., and Lancaster, M, J. (2008). Barium Strontium Titanate Thin Film Varactors for Room-Temperature Microwave Device Applications. *J Phys. D: Appl. Phys.*, Vol.41, No.6, (June 2008), pp. 063001, ISSN 0022-3727

Baringay, C. K. & Dey, S. K. (1992). Observation of sol-gel solid phase epitaxial growth of ferroelectric $Pb(Nb,Zr,Ti)O_3$ thin films on sapphire. *Appl. Phys. Lett.*,Vol. 61, No. 11, (September1992), pp.1278-1280, ISSN 0003-6951

Bochu, B., Deschizeaux, M. N., and Joubert, J. C., (1979). Synthése et Caratérisation d'une Série de Titanate Pérowskite Isotypes de $[CaCu_3](Mn_4)O_{12}$. *J Solid State Chem.*, Vol.29, No.2, (August 1979), pp. 291-298, ISSN 0022-4596

Chung, U. C., Elissalde, E., Estournes, C., Pate, M., and Ganne, J. P. (2008). Low Loss, Highly Tunable $Ba_{0.6}Sr_{0.4}TiO_3$/MgO Composites. *Appl. Phys. Lett.* Vol.92, No.4, (January 2008), pp. 042902, ISSN 0003-6951

Cole, M. W., Joshi, P. C., Ervin, M. H., and Pfeffer, R. L. (2000). The Influence of Mg Doping on the Materials Properties of BST Thin Films for Tunable Device Applications. *Thin Solid Films*, Vol. 374, No.1, (October 2000), pp. 34-41, ISSN 0040-6090

Copel, M., Baniecki, J. D., Duncombe, P. R., and Shaw, T. M.(1998). Compensation Doping of $Ba_{0.7}r_{0.3}TiO_3$ Thin Films. *Appl. Phys. Lett.* Vol.73, No.13, (September 1998), pp. 1832-1834, ISSN 0003-6951

Courrèges, S., Zhao, Z. Y., Choi, K., Hunt, A. T., and Papapolymerou, J. (2010) Electrically Tunable Ferroelectric Devices for Microwave Applications, In: *Microwave and Millimeter Wave Technologies from Photonic Bandgap Devices to Antenna and Applications*, Igor Minin, pp. 1-20, InTech, ISBN: 978-953-7619-66-4, Vienna, Austria

Dawber, M., Rabe, K. M., and Scott, J. F. (2005). Physics of Thin Film Ferroelectric Oxides. *Reviews of Modern Phys.*, Vol. 77, No.4, (December 2005), pp. 1083-1130, ISSN 0034-6861

Deschanvres, A., Raveau, B., and Tollemer, F. (1967). Replacement de Metal Bivalent par le Cuivre Dans les Titanates de Type Perowskite. *Bull. Soc. Chim. Fr.*, pp. 4077-4078, ISSN 0037-8968

Dimos, D. and Mueller, C. H. (1998). Perovskite Thin Films for High Frequency Capacitor Applications. *Ann. Rev. Mater. Sci.*, Vol.28, No.1, (January 1998). pp. 397-419, ISSN 1531-7331

Dimos, D., Schwartz, R. W., and Lockwook, S. J. (1994). Control of Leakage Resistance in Pb(Zr,Ti)O3 Thin Films by Donor Doping. *J Am. Ceram. Soc.* Vol. 77, No.11, (November 1994), pp. 3000-3005, ISSN 0002-7820

Gevorgian, S. S. and Kollberg, E. L. (2001). Do We Really Need Ferroelectrics in Paraelectric Phase Only in Electrically Controlled Microwave Devices. *IEEE Trans. Microwave Theory Techn.*, Vol.49, No.11 (November 2001), pp. 2117-2124, ISSN 0018-9480

Heindl, P., Srikanth, H., Weller, T., Tatarenko, A. S., and Srinivasan, G. (2007). Structure, Magnetism, and Tunable Microwave Properties of Pulsed Laser Deposition Growth Barium Ferrite/Barium Strontium Titanate Bilayer Films. *J Appl. Phys.* Vol. 101, No.9, (July 2007), pp. 09M503, ISSN 0021-8979

Home, C. C., Vogt, T., Shapiro, S. M., Wakimoto, S., and Ramirez, A. P. (2001). Optical Response of High Dielectric Constant Perovskite-Related Oxide. *Science*, Vol.293, No.5530, (July 2001), pp. 673-676, ISSN 0036-8075

Hwang, C. S., Lee. B. T., Kang, C. S., Lee, K. H., Cho, H., Hideki, H., Kim, W. D., Lee, S. I., and Lee, M. Y. (1999), Depletion Layer Thickness and Schorttky Type Carrier Injection at the Interface Between Pt Electrode and $(Ba,Sr)TiO_3$ Thin Films. *J Appl. Phys.*, Vol.85, No.1, (January 1999), pp. 287-295, ISSN 0021-8979

Hwang, K. S., Manabe, T., Nagahama, T., Yamaguchi, I., Kumagai, T., and Mizuta, S. (1999). Effect of Substrate Material on the Crystallinity and Epitaxy of $Pb(Zr,Ti)O_3$ Thin Films. *Thin Solid Films* Vol. 347, No.1-2, (June 1999), pp. 106-111, ISSN 0040-6090

Hunt, A. T., Carter, W. B., and Cochran, J. K. (1993). Combustion Chemical Vapor Deposition: A Novel Thin Film Deposition Technique. *Appl. Phys. Lett.*, Vol.63, No.2, (July 1993), pp. 266-268, ISSN 0003-6951

Hunt, A. T., Cochran, J. K., and Carter, W. B. (1997). Combustion Chemical Vapor Deposition of Films and Coatings. U.S. Patent No. 5,652,021

Hunt, A. T., Hwang, T. J., and Shao, H. (1999). Combustion Chemical Vapor Deposition of Phosphate Films and Coatings. U.S. Patent No. 5,858,465

Im, J., Auciello, O., Streiffer, S. K., and Krauss, A. R. (2000). Composition Control of Magnetron-Sputter-Deposited $(Ba_xSr_{1-x})Ti_{1+y}O_{3+z}$ Thin Films for Voltage Tunable Devices. *Appl. Phys. Lett.* Vol.76, No.5, (January 2000), pp. 625-627, ISSN 0003-6951

Kang, D. H., Lee, S. Y., Kim, Y. H., Gil, S. K., and Park, D. S. (2006), Control of Dispersion Frequency of $BaTiO_3$-based Ceramics Applicable to Thin Absorber for Millimeter Electromagnetic Wave. *J Euro. Ceram. Soc.*, Vol. 26, No.10-11, (October 2006), pp. 2169-2173, ISSN 0955-2199

Katiyar, R. S., Jain, M., Miranda, F. A., and Van Keuls, F. W. (2005). Comparative Studies of Ferroelectric Thin Films for High Frequency Phase Shifter Applications. *Integrated Ferroelectrics*, Vol.71, No.1, (January 2005) pp. 11-19, ISSN 1058-4587

Kim, B. K., Lee, H. S., Lee, J. W., Lee, S. E., and Cho, Y. S. (2010). Dielectric and Grain-Boundary Characteristics of Hot Pressed $CaCu_3Ti_4O_{12}$. *J Am. Ceram. Soc.* Vol.93, No.9, (September 2010), pp. 2419-2422, ISSN 0002-7820

Kim, H. H., Kim, S. T., and Lee, W. J. (1998). The Effects of In-situ Pretreatments of the Substrate Surface on the Properties of PLZT Films Fabricated by a Multi-Target Sputtering Method. *Thin Solid Films* vol. 324, No.1-2, (July 1998), pp.101-106, ISSN 0040-6090

Kim, W. S., Ha, S. M., and Kim, C. E. (1999). The Effects of Cation Substitution on the Ferroelectric Properties of Sol-Gel Derived PZT Thin Films for FRAM Application. *Thin Solid Films* Vol. 355-356, pp. 531-535, No.1, (November 1999), ISSN 0040-6090

Kobune, M., Fuijii, S., Takayama, R., and Tomozawa, A. (1996). Preparation and Pyroelectric Properties of $(Pb,La)(Zr,Ti)O_3$ (PLZT Thin Films. *Jpn. J Appl. Phys.* Vol. 35, No.9B, (September 1996), pp. 4980-4983, ISSN 0021-4922

Li, M., Shen, Z. J., Nygren, M., Feteira, A., Sinclair, D. C., and West, A. R. (2009). Origin(s) of the Apparent high Permittivity in CaCu3Ti4O12 Ceramics: Clarification on the Contributions from Internal Barrier Layer Capacitor and Sample-Electrode Contact Effects. J. Appl. Phys., Vol.106, No.10, (November 2009), pp. 104106, ISSN 0021-8979

Liu, H., Gong, X. G., Liang, L. E., Li, X. D., Zhu, J. G., and Pu, Z. H. (2007). Enhanced Dielectric and Ferroelectric Properties of $Pb(Zr_{0.8}Ti_{0.2})TiO_3/Pb(Zr_{0.2}Ti_{0.8})TiO_3$ Multilayer Films. *Appl. Phys. Lett.* Vol.91, No.12, (September 2007), pp. 122906, ISSN 0003-6951

Lu, X. Y., Wang, B., Zheng, Y., and Li, C. L. (2008). Adjustable Ferroelectric Properties in Ferroelectric/Paraelectric Trilayers. *J Phys. D: Appl. Phys.* Vol. 41, No.3, (February 2008), pp. 035303, ISSN 0022-3727

Mauray, D., Singh, D. P., Agrawal, D. C., and Mohapatra, Y. N. (2008). Preparation of High Dielectric Constant Thin Films of $CaCu_3Ti_4O_{12}$ by Sol-Gel. *Bull. Mater. Sci.* Vol.31. No.1, (February 2008), pp.55-59, ISSN 0250-4707

Misirlioglu, I., B., Akcay, G., Zhong, S., and Alpay, S. P. (2007), Interface Effects in Ferroelectric Bilayers and Heterostructures. *J Appl. Phys.* Vol. 101, No.3, (February 2007), pp. 036107, ISSN 0021-8979

Natori, K., Otani, D., and Sano, N. (1998), Thickness Dependence of the Effective Dielectric Constant in a Thin Film Capacitor. *Appl. Phys. Lett.*, Vol. 73, No.5, (August 1998), pp. 632-634, ISSN 0003-6951

Pintilie, L., Boldyreva, K., Alexe, M., and Hesse, D. (2008). Capacitance Tuning in Antiferroelectric Ferroelectric $PbZrO_3$-$Pb(Zr_{0.8}Ti_{0.2})TiO_3$ Epitaxial Multilayers. *New J Phys.* Vol. 10, No.1, (January 2008), pp. 013003, ISSN 1367-2630

Polla, D. L. and Francis, L. F. (1998). Processing and Characterization of Piezoelectric Materials and Integration into Microelectromechical Systems. *Ann. Rev. Mater. Sci.* Vol. 28, No.1, (January 1998), pp. 563, ISSN 1531-7331

Prakash, B. S., Varma, K. B., and Maglione, M. (2008). Deposition and Dielectric Properties of CCTO Thin Films Deposited on $Pt/Ti/SiO_2/Si$ Substrates using RF Magnetron Sputtering. Thin Solid Films, Vol.516, No.10, (), pp. 2874-2880, ISSN 0040-6090

Ramesh, R., Aggarwal, S., and Auciello, O. (2001). Science and Technology of Ferroelectric Films and Heterostructures for Non-volatile Ferroelectric Memories. *Mater. Sci. Eng. R* Vol. 32, No.6, (April 2001), pp. 191-236, ISSN 0927-796X

Ramirez, A. P., Subramanian, P. A., Gardel, M., Blumberg, G., Li, D., Vogt, T., and Shapiro, S. M. (2000). Giant Dielectric Constant Response in a Copper Titanate. *Solid State Communications*, Vol.115, No.5, (June 2000), pp. 217-274, ISSN 0038-1098

Rukmini, H. R., Choudhary, R. N. P., and Rao, V. V. (1999). Structural and Dielectric Properties of $Pb_{0.9}(La,K)_{0.09}(Zr_{0.65}Ti_{0.35})_{0.9775}O_3$. *J Mater. Sci.* Vol.34, No.19, (October 1999), pp. 4815-4819, ISSN 0022-2641

Scott, J. F. (1999). Depletion Width in $SrTiO_3$ and $BaxSr_{1-x}TiO_3$ Films. *Ferroelectrics*, Vol.232, No.1, (January 1999), pp. 25-34, ISSN 0015-0193

Sinclair, D. C., Adams, T. B., Morrison, F. D., and West, A. R. (2002). $CaCu_3Ti_4O_{12}$: One-Step Internal Barrier Capacitor. *Appl. Phys. Lett.*, Vol.80, No.12, (March 2002), pp. 2153-2155, ISSN 0003-6951

Sinnamon, L. J., Saad, M. M., Bowman, R. W., and Gregg, J. M. (2002). Exploring Grain Size as a Cause for "Dead-Layer" Effects in Thin Film Capacitors. *Appl. Phys. Lett.*, Vol.81. No.4, (July 2002), pp.703-705, ISSN 0003-6951

Song, Z. T., Chong, N., Chan, H. L. W., and Choy, C. L. (2001) Electrical and Pyroelectric Properties of In-plane Polarized Lead Lanthanum Titanate Thin Films. *Appl. Phys. Lett.* Vol.79, No.5, (July 2001), pp. 668-670, ISSN 0003-6951

Streiffer, S. K., Basceri, C., Parker, C. B., Lash, S. E., and Kingon, A. I. (1999) Ferroelectricity in Thin Films: The Dielectric Response of Fiber-Textured $(Ba_xSr_{1-x})Ti_{1+y}O_{3+z}$ Thin Films Grown by Chemical Vapor Deposition. *J Appl. Phys.*, Vol.86, No.8, (October 1999), pp. 4565-4567, ISSN 0003-6951

Subramanian, M. A, Li, D., Duan, N., Reisner, B. A., and Sleight, A. W. (2000). High Dielectric Constant in $ACu_3Ti_4O_{12}$ and $ACu_3Ti_4FeO_{12}$. *J Solid State Chem.*, Vol.151, No.2, (May 2000), pp.323-325, ISSN 0022-4596

Subramanian M. A. and Sleight, A. W. (2002). $ACuTi_4O_{12}$ and $ACu_3Ru_4O_{12}$ Perovskites: High Dielectric Constants and Valence Degeneracy. *Solid State Sciences*, Vol.4, No.3, (March 2002), pp. 347-351, ISSN 1293-2558

Tagantsev, A. K, Sherman, V. O, Astafiev, K. F. , Venkatesh, J., and Setter, N. (2003). Ferroelectric Materials for Microwave Tunable Applications. *J Electroceramics*, Vol. 11, No.1, (September 2003), pp. 5-66, ISSN 1385-3449

Takeuchi, I., Chang, H., Gao, C., Xiao, X. D., Downes, M. J., and Venkatesan, T. (1998). Combinatorial Synthesis and Evaluation of Epitaxial Ferroelectric Device Libraries. *Appl. Phys. Lett.*, Vol.73, No.7, (August 1998), pp. 894-896, ISSN 0003-6951

Xu, B., M., Rolcawich, R., G., Trolier-McKinstry, S., Ye, Y., H., and Cross, L. E. (1999) Sensing Characteristics of In-plane Polarized Lead Zirconate Titanate Thin Films. *Appl. Phys. Lett.*, Vol. 75, No.26, (December 1999), pp. 4180-4182, ISSN 0003-6951

Xu, Y. (1991). *Ferroelectric Mater. & Their Appl.*, North Holland, ISBN 0-444-88354-1, Amsterdam, The Netherlands

Zhong, S., Alpay, S. P., Cole, M. W., Ngo, E., Hirsch, S., and Demaree, J. O. (2007). Highly Tunable and Temperature Insensitive Multilayer Barium Strontium Titanate Films. *Appl. Phys. Lett*. Vol. 90, No.9, (February 2007), pp. 092901, ISSN 0003-6951

Zhou, C. and Newns, D. M. (1997). Intrinsic Dead Layer Effect and the Performance of Ferroelectric Thin Film Capacitors. *J Appl. Phys.*, Vol.82, No.6, (September 1997), pp. 3081-3088, ISSN 0021-8979

Zhu, B. P., Wang, Z. Y., Zhang, Y., Yu, Z. S., Shi, J., and Xiong, R. (2008). Low Temperature Fabrication of the Giant Dielectric Material $CaCu_3Ti_4O_{12}$ by oxalate Coprecipitation Method, *Mater. Chem. Phys.* Vol.113, No.2-3, (February 2008), pp. 746-748, ISSN 0254-0584

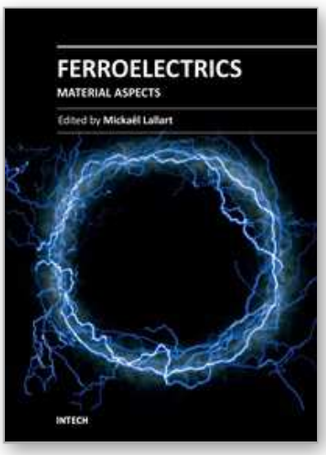

Ferroelectrics - Material Aspects

Edited by Dr. MickaÃ«l Lallart

ISBN 978-953-307-332-3
Hard cover, 518 pages
Publisher InTech
Published online 24, August, 2011
Published in print edition August, 2011

Ferroelectric materials have been and still are widely used in many applications, that have moved from sonar towards breakthrough technologies such as memories or optical devices. This book is a part of a four volume collection (covering material aspects, physical effects, characterization and modeling, and applications) and focuses on ways to obtain high-quality materials exhibiting large ferroelectric activity. The book covers the aspect of material synthesis and growth, doping and composites, lead-free devices, and thin film synthesis. The aim of this book is to provide an up-to-date review of recent scientific findings and recent advances in the field of ferroelectric materials, allowing a deep understanding of the material aspects of ferroelectricity.

How to reference

In order to correctly reference this scholarly work, feel free to copy and paste the following:

Yongdong Jiang, Yongqiang Wang, Kwang Choi Deepika Rajamani and Andrew Hunt (2011). BST and Other Ferroelectric Thin Films by CCVD and Their Properties and Applications, Ferroelectrics - Material Aspects, Dr. MickaÃ«l Lallart (Ed.), ISBN: 978-953-307-332-3, InTech, Available from: http://www.intechopen.com/books/ferroelectrics-material-aspects/bst-and-other-ferroelectric-thin-films-by-ccvd-and-their-properties-and-applications

INTECH
open science | open minds

InTech Europe
University Campus STeP Ri
Slavka Krautzeka 83/A
51000 Rijeka, Croatia
Phone: +385 (51) 770 447
Fax: +385 (51) 686 166
www.intechopen.com

InTech China
Unit 405, Office Block, Hotel Equatorial Shanghai
No.65, Yan An Road (West), Shanghai, 200040, China
中国上海市延安西路65号上海国际贵都大饭店办公楼405单元
Phone: +86-21-62489820
Fax: +86-21-62489821

© 2011 The Author(s). Licensee IntechOpen. This chapter is distributed under the terms of the Creative Commons Attribution-NonCommercial-ShareAlike-3.0 License, which permits use, distribution and reproduction for non-commercial purposes, provided the original is properly cited and derivative works building on this content are distributed under the same license.

IntechOpen

IntechOpen